Acta Materialia 181 (2019) 584–594

Contents lists available at ScienceDirect

Acta Materialia

journal homepage: www.elsevier.com/locate/actamat

Full length article

Thermodynamics of solute capture during the oxidation of multicomponent metals

Q.C. Sherman, P.W. Voorhees, L.D. Marks*

Department of Materials Science and Engineering, Northwestern University, Evanston, IL 60208, USA

ARTICLE INFO

Article history:
Received 24 July 2019
Revised 16 September 2019
Accepted 21 September 2019
Available online 25 September 2019

Keywords:
Phase transformations
Oxidation
Corrosion
Thermodynamic modeling
Density functional theory

ABSTRACT

In the classical theories of oxidation of metals it is assumed that the interface between the oxide and metal is in thermodynamic equilibrium. However, in many cases this is not true, the oxide grows too fast or the fluxes through the interface are too large for local interfacial equilibrium to exist, leading to nonequilibrium solute capture. We present a thermodynamic analysis using both an available database as well as density functional theory calculations of the thermodynamic conditions for this during the oxidation of Ni–Cr alloys. The analysis indicates that nickel atoms can be captured in the rocksalt or corundum crystallographies for a very wide range of compositions, consistent with recent experimental observations. The density functional theory analysis also provides information about the electronic structure of these oxides which is important to understand their properties, and also indicates that interpretation of spectroscopic data is not simple as mixed valence states as well as Cr^{4+} can occur under oxidizing conditions. We point out that across at least the first transition row of elements the thermodynamic conditions for nonequilibrium solute capture can easily be met.

1. Introduction

A phase transformation occurs when a system transitions from an initial state to either a lower energy metastable state or the true equilibrium state. During a diffusional phase transformation, the state variables in the system must transition from their far-field values in the bulk phases to some value at the interface between the phases, which is typically determined by an assumption of local thermodynamic equilibrium at the interface. The profiles of the state variables between the bulk and interfacial values are then governed by thermodynamically consistent diffusion equations. In the classic Wagner model of oxidation, the ionic defect concentrations at both the gas-oxide and oxide-metal interfaces are set by local equilibrium assumptions, with a quasi-steady-state diffusion field in between that drives the interface motion [1]. This is valid for a slowly growing, relatively thick oxide film where the interface does not significantly differ from the metal or oxide, and leads to an expectation that the oxide films will be dominated by the thermodynamically stable oxide phases.

Consistent with this, thermodynamically favored oxide phases are commonly assumed to form (e.g. [2–5]), or phases which are stable in Pourbaix diagrams [6]. In nickel-chromium alloys these would be pure nickel oxide and chromia [7–11], which may be enriched with alloying elements [12–15]. However, as first pointed out by Wagner [16,17] and further developed by Wood [18], often the thermodynamically favored oxides do not form. Sometimes a metastable variant is present that converts to the thermodynamically stable form with slower growth kinetics [19–22], suggesting Ostwald's step rule [23–27].

However, both in the early stages of oxidation at elevated temperature and in many cases of aqueous corrosion, the oxide film is thin, and the assumption of local equilibrium may not hold. Indeed, based upon extensive characterization supplemented by thermodynamic and density functional modeling, we have recently reported that there are significant deviations from local equilibrium in many cases, and inferred that this may be very common [28]. There are similarities to conventional solute trapping [29], but also significant differences so we termed this as nonequilibrium solute capture. The interpretation of the experimental results was based upon an extension of conventional solute trapping during solidification, and involved two components, a kinetic and a thermodynamic condition. If the thermodynamic condition holds then solute capture can occur; if the kinetic condition also holds then it does occur.

The intent of this note is to expand in more detail on the thermodynamic conditions both in general and for the specific case of the Ni–Cr system, combining extensions of the available thermodynamic models with density functional theory (DFT) calculations

* Corresponding author.
E-mail address: L-marks@northwestern.edu (L.D. Marks).

https://doi.org/10.1016/j.actamat.2019.09.043
1359-6454/

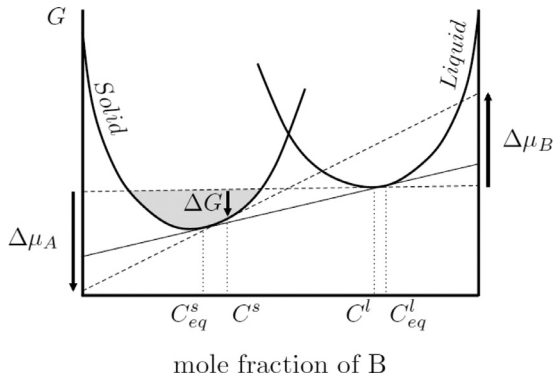

Fig. 1. Schematic of free energy vs. composition curves and the associated driving force for solidification of an alloy AB. When the interface motion is very slow, the interfacial compositions of the solid and liquid will approach C^s and C^l, respectively. However it is possible to form solid of any composition in the shaded region from a liquid of initial composition C^l. The changes in chemical potential for A and B, $\Delta\mu_A$ and $\Delta\mu_B$, when forming solid of composition C^s from liquid of composition C^l, as well as the associated driving force ΔG, are shown using a graphical construction [32]. The chemical potential of component B increases during the phase transformation, however the driving force is positive.

to cross-validate them. We will also provide crystallographic information about the relevant structures, to explain the local chemistry and electronic structure; these are important because they provide information on the properties of the oxides. The structure of this note is as follows. In the next section we will provide some general background to both the general concepts of nonequilibrium interfaces and the oxides of relevance. This is followed by a brief description of the numerical methods used, primarily for the density functional calculations. After this an analysis will be presented combining both conventional thermodynamics and the density functional results, including descriptions of the various metastable phases considered in terms of their local chemistry and electronic structure. The conclusions of the thermodynamic analysis is that nonequilibrium solute capture of nickel can occur in both rocksalt and corundum crystallographies containing chromium as the dominant metal for a very wide range of compositions, in agreement with experimental results. Later papers will examine in more detail the coupling between the effective interface velocity and composition [30], as well as further experimental and theoretical details of the electronic nature of the nonequilibrium solute captured oxide [31].

2. Background

2.1. Nonequilibrium interfaces, solute trapping and capture

We will first describe solute trapping during solidification, as our formulation of nonequilibrium solute capture stems from it. Baker and Cahn [29,32] were the first to describe in detail the thermodynamic conditions for deviations from equilibrium at a moving interface in a multi-component system during a rapid phase transformation. One of their principle insights was that a solute can experience an increase in chemical potential across the moving interface during solidification—so long as the total free energy change for the phase transformation is negative. The solute is said to be "trapped" in the higher energy state in the growing phase. This is illustrated schematically in Fig. 1, where the chemical potential of component B increases during the solidification of a liquid of composition C^L to solid of composition C^s. Solute trapping will only occur, however, if an additional kinetic constraint is met: the interface velocity must be large compared to a solute diffusivity term that is related to exchange of different types of atoms in the solid. A number of models were subsequently developed to describe the dependence of the interface compositions during solidification as a function of interface mobility and solute diffusivity, which have been reviewed by Boettinger et al. [33], and more recently by Galenko [34]. In the limit of zero diffusivity in the growing phase, perhaps the best known of these is the model of Aziz [35], where the partition coefficient in the dilute limit is given by

$$k(\bar{V}) \equiv {C^S}/{C^L} = \frac{k_0 + \bar{V}}{1 + \bar{V}} \tag{1}$$

where the quantities C^S and C^L are the mole fractions of solute in the solid and liquid at the interface, k_0 is the equilibrium partition coefficient, $\bar{V}$ is a nondimensionalized velocity defined as $\bar{V} = V\beta_0$ with V the interface velocity and $\beta_0 = a/D$ a characteristic inverse velocity from the ratio of a diffusional hopping distance a and D the solute diffusivity across the interface. Eq. (1) gives the partition coefficient during the solidification of dilute melts. If, in addition, a thermodynamic description of the system and interface mobility are known, then in a binary alloy the nonequilibrium interface compositions can be calculated.

Nonequilibrium solute capture particularly during the formation of an oxide has similarities, but is not the same [28]. First, taking an oxygen atom (which is picked such that it does not move with respect to the lattice) at the interface as the reference origin, growth of the oxide can occur by a number of atomic mechanisms:

a) The formation of oxygen vacancies at the interface which then diffuse to the outer surface; in this case the interface moves into the alloy.
b) The diffusion of oxygen interstitials in from the outer surface. Again, the interface moves into the alloy.
c) The creation of cation vacancies at the outer surface which then diffuse to the metal/oxide interface and then cross into the alloy. In this case the oxide/metal interface is stationary with respect to the reference atom and growth occurs at the outermost surface.
d) The formation of cation interstitials in the oxide at the interface (by transfer from the alloy) which then move to the outer surface. Again, the interface is stationary with respect to the reference atom and growth occurs at the outermost surface.

The "velocity" term in Eq. (1) must take account of the relevant fluxes across the interfaces, i.e. for a planar interface in a binary alloy [36]

$$V(C - c^m) = j^o \; - J^M \tag{2}$$

where V is the velocity normal to the interface, C the concentration of material transferred across the interface, c^m the concentration in the metal, j^o the flux across the oxide/metal interface and J^M the flux in the metal at the interface. Note that unlike solute trapping, the oxide/metal interface can be stationary with respect to the reference atom, hence there are differences. In this case, capture can occur due to the fluxes of atoms across the interface [3], as will be discussed in more detail elsewhere [30].

In addition to the above differences in the velocity term, a second difference is in the energetics. In solute trapping the chemical potential of the trapped solute increases whereas that of the solvent decreases. In a multicomponent metal alloy AB which is oxidizing to some compound of chemical composition AB_xO_y, in almost all cases the free energy of formation of both the oxides of A and B will be negative, as will be shown later for the specific case of nickel-chrome oxides, so there is no trapping in the classical sense, but there can be interfacial nonequilibrium.

Yet a third difference is at the atomic scale. During solidification, for instance of a metal, a more ordered arrangement of metal atoms develops with the free energy change dominated by the metallic bonding. In contrast oxides, almost without exception, contain close-packed arrangements of oxygen atoms with the

much smaller cations in the interstices, and the free energy change during oxidation is controlled by a combination of ionic and covalent bonding between the small cations and the larger oxygen atoms as well as non-bonding repulsions between the oxygen atoms. The oxygen atom arrangement dictates the crystallography, for instance an fcc arrangement for a rocksalt oxide (space group $Fm\bar{3}m$) which contrasts with an hcp oxygen atom arrangement for a corundum oxide (space group $R\bar{3}c$). Note that we are very deliberately defining the structures by the structure type and their crystallographic space groups, not by the chemical composition; this is critical to reduce confusion.

A fourth difference concerns the factors that control the terms Eq. (1). It is generally accepted that the diffusivity term in this equation during solidification is mainly determined by the much faster diffusion in the liquid. In contrast, during oxide formation (solute capture) to what extent site exchange across the interface similar to Zener-type cation redistribution in oxides (e.g. [37–42]) dominates versus diffusion in the metal is not as yet clear, as atom movement can only occur between allowed sites of a lattice.

Lastly, metal/oxide interfaces are not as simple as the typical metal/metal interfaces that have been considered in most solute trapping problems. For instance, interfaces involving crystallographically polar directions of the oxide will be very different from non-polar directions, as is well established for oxide surfaces where there can be considerable changes in local co-ordination and structure. In contrast, for the typical high temperature conditions of metal solute trapping during rapid solidification there is usually very little anisotropy or crystallographic dependence of interface properties.

Solute trapping and solute capture are not the same. Returning to the primary focus of this paper, an important question is under what conditions is the free energy change during the formation of an oxide from a metal of a given composition negative – for all compositions and crystallographies or only for a few? If there are many oxides compositions and crystallographies which satisfy this free energy conditions then a plethora of oxides is possible. As we will see this is what happens in the NiCr system.

2.2. NiCr oxidation

There are three established thermodynamically stable oxide phases in the oxidation of NiCr alloys: rocksalt NiO ($Fm\bar{3}m$), corundum Cr_2O_3 ($R\bar{3}c$), and the spinel $NiCr_2O_4$ ($Fd\bar{3}mZ$). As mentioned earlier we are deliberately specifying here both the crystallography (e.g. rocksalt $Fm\bar{3}m$) as well as the chemical composition as both are needed. In oxides nickel can have either 2+ or 3+ oxidation states while chromium prefers 3+ but could be 2+ or 4+. At equilibrium these oxide structures only contain a small amount of substitutional nickel and chromium, and rocksalt NiO can contain some nickel vacancies associated with Ni^{3+}. Chromium is more electropositive than nickel, and as a result chromium oxides have a larger thermodynamic driving force for formation than their nickel counterparts. Therefore we would expect the oxides to form in the order $Cr_2O_3 \rightarrow NiCr_2O_4. \rightarrow NiO$. This is not what happens.

In addition to these stable phases, a metastable (at STP) Ni_2O_3 corundum phase ($R\bar{3}c$) as well as a spinel (or inverse-spinel) Ni_3O_4 are well established, both of which contain Ni^{3+} and can be formed under strong oxidizing conditions or under electron irradiation [43]. There is very tenuous experimental evidence for a rocksalt CrO ($Fm\bar{3}m$) oxide containing Cr^{2+}; for completeness we note that there is a deep eutectic in the Cr–O phase diagram near this composition [44]. Some work has attempted to produce a half-metal distorted perovskite $NiCrO_3$ [45–48], but based upon our analysis later a distorted perovskite would be significantly higher in energy. As will be shown, these compounds that form under higher oxidizing conditions contain combinations of Ni^{2+} and Cr^{4+}.

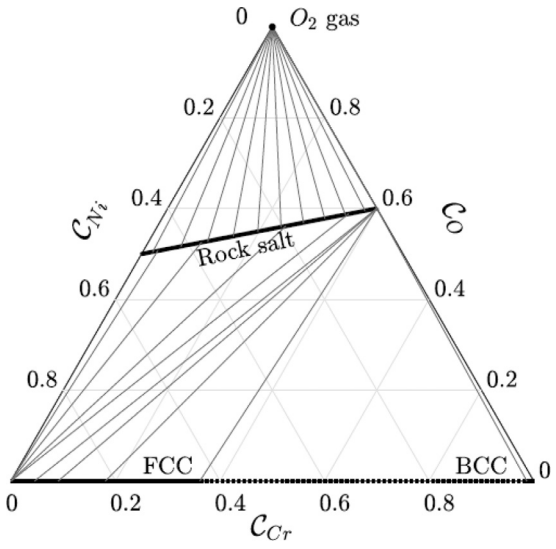

Fig. 2. Ternary phase diagram of the Ni–Cr–O system at $T = 1000$ K and atmospheric pO_2 with the corundum and spinel oxide phases removed, calculated from [44]. The light grey lines are tie lines in the two-phase regions. The dotted line on the C_{Cr} axis is the two-phase region in the pure alloy.

3. Thermodynamic description

Turning now to the free energy changes, we will divide the analysis into two parts. The first will be from a conventional thermodynamic database, the second will be from density functional theory calculations which will include details about the electronic structure and local chemistry.

3.1. Thermodynamic database

We use the assessment of Taylor and Dinsdale [44] to calculate the thermodynamic properties of the Ni–Cr–O system. We will limit ourselves here to combining the fcc alloy (excluding any bcc phases), the rocksalt Ni_XCr_YO ($Fm\bar{3}m$) phase and the spinel as a line compound; see Fig. 2 for the ternary phase diagram at 1000 K and atmospheric oxygen for the rocksalt and metal phases. The thermodynamic database (TD) contains all the relevant free energy and entropy terms of the different compounds, including the magnetic contributions for the fcc alloys and the antiferromagnetic oxides NiO and Cr_2O_3. We note that valence neutrality was assumed in the analysis of Taylor and Ginsdale. The database does not contain magnetic terms for the spinel; we will return to the magnetic ordering of the spinel later in the DFT section. We note that there is considerable scatter in the available thermodynamic data for the spinel [49].

We have excluded the TD assessment for nickel substitution in chromia since this deviates too much from the DFT results which are described later. Taylor and Dinsdale [44] had very little data to work with, tested both lattice and interstitial models then assumed an interstitial model. Unfortunately, this was the wrong choice. Crystallographically chromia can be written as $Cr_2V^NO_3$ where V^N are neutral vacant sites as only two-thirds of the octahedral sites are occupied. As will be described in the DFT section, the correct approach is site substitution of Ni^{3+} or Ni^{2+} at the occupied chromium and neutral vacant sites with antiferromagnetic ordering below.

A second point about the TD assessment is that while it is accurate for what it includes, if it omits a reaction or phase then inaccuracies are present. The DFT calculations (see later) indicate that Cr^{4+} can form from the oxidation of Cr^{3+} by Ni^{3+}, i.e. the reaction $Ni^{3+} + Cr^{3+} \rightarrow Ni^{2+} + Cr^{4+}$. The possibility of Cr^{4+} was not

included in the assessment. However, the free energy of this reaction is not large so it will not significantly change the overall conclusions since, as we will see, the dominant free energy changes are an order of magnitude later.

The molar Gibbs free energy of the fcc NiCr alloy in the TD assessment is given by:

$$G^M = \sum_i \left[C_i^M G_i^0 + RTC_i^M lnC_i^M\right] + G^{ex} + G^{mag} \quad \text{for i} = \text{Ni, Cr} \tag{3}$$

where C_i^M is the mole fraction of species i in the alloy, G_i^0 is the free energy of species i in the fcc structure, and G^{ex} and G^{mag} are the excess free energy and magnetic contribution to the Gibbs free energy of the phase. Oxygen solubility is not modeled in the metal phase.

Taylor and Ginsdale used the compound-energy formalism, reviewed by Hillert [50], to describe the molar free energy of the rocksalt oxide phase ($Fm\bar{3}m$) with subspecies [Ni^{2+}, Ni^{3+}, Cr^{3+}, Va][O^{2-}], where Va is a cation vacancy. The molar free energy of the rocksalt unit cell is given by:

$$G^{RS} = \sum_i \chi_i G_i^o + RT\chi_i ln\chi_i \tag{4}$$

where χ_i is the site fraction of species i (=Ni^{2+}, Ni^{3+}, Cr^{3+}, Va) on the cation sublattice and G_i^o is the Gibbs free energy of the compound. (Based upon the DFT results, in many cases the Ni^{3+} should be replaced by Cr^{4+}; we will not consider this further here.) To reduce the number of variables, there are two additional constraints:

a) The site fractions are coupled by structure conservation:

$$\chi_{Ni^{2+}} + \chi_{Ni^{3+}} + \chi_{Cr^{3+}} + \chi_{V_a} = 1 \tag{5}$$

b) The site fractions of Ni^{3+} and Cr^{3+} are coupled to the vacancy site fraction by valence neutrality:

$$\chi_{Ni^{3+}} + \chi_{Cr^{3+}} = 2\chi_{V_a} \tag{6}$$

We are deliberately using here the more correct term “valence neutrality” rather than the commonly used “charge neutrality”, as the latter is only correct in the limit of a completely ionic oxide; valence and electrostatic charges are different. Converting to chemical potentials,

$$G^{RS} = \mu_{Ox} + (\chi_{Ni^{3+}} + \chi_{Ni^{3+}})\mu_{Ni} + \chi_{Cr^{3+}}\mu_{Cr} \tag{7}$$

for a given value of the oxygen chemical potential in the oxide. In general, the oxygen chemical potential will not be uniform across the oxide, and can also change at the interface depending upon whether it is polar or non-polar. Since we are only considering the solute capture at the oxide-metal interface here, we do not attempt to determine details of the spatial distribution of the oxygen chemical potential, rather we will use the value of the oxygen chemical potential as a parameter in units of the equivalent oxygen partial pressure and the corresponding chemical potential from a thermodynamic database [51].

One slightly complicated issue is the units of the plots, which will be discussed later in more detail. For the moment we will normalize per metal atom, in which case the free energy of the oxide G^{Ox} can be written as

$$G^{Ox} = (G^{RS} - \mu_{Ox})/(1 - \chi_{V_a}) \tag{8}$$

The free energy G^{Ox}, when plotted as a function of composition, is directly comparable with the composition dependent molar free energy of the alloy, G^{Ox}, and can be used to calculate a graphical construction of the driving force for oxidation, see Fig. 3. This shows the free energy change on forming an oxide with various compositions from a metal of composition C^M. Within the thermodynamic database where the free energies are continuous functions, the free energy change is measured from a tangent constructed at C^M to the free energy curve. It is clear the free energy of the oxide is below the tangent for any composition of the oxide and thus there is a wide range of oxide compositions that can form.

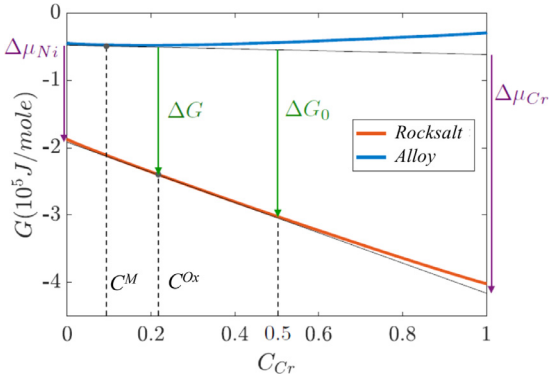

Fig. 3. Free energy versus composition curves for the alloy and rocksalt oxide at $T = 1000$ K and atmospheric oxygen effective pressure. The free energy is plotted in units of joules per mole of nickel and chromium. The oxygen in the oxide is in equilibrium with the atmosphere. The driving force for oxidation, ΔG, for alloy composition C^M and oxide composition C^{Ox} is constructed graphically. It is given by the vertical distance between the tangent line of the alloy free energy curve at C^M and the free energy curve of the rocksalt oxide. A characteristic driving force ΔG_0 for the formation of oxide of composition C_{Cr}=0.5 from a metal of composition C_{Cr}=0.1 also shown. The chemical potential of each component decreases upon the formation of the oxide, as shows by the arrows at C_{Cr}=0,1.

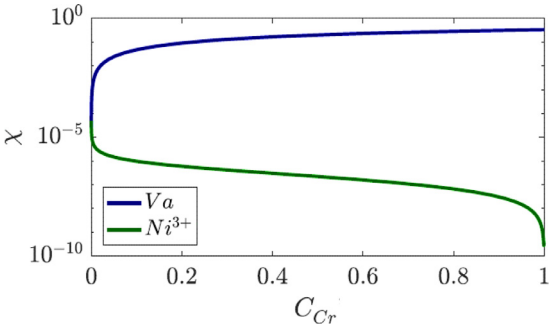

Fig. 4. Vacancy and Ni3+ concentration in the rocksalt oxide as a function of chromium content at $T = 1000$ K and atmospheric effective oxygen pressure. The concentration curves satisfy valence neutrality and oxygen equilibrium with the gas phase.

There are implicit vacancy and Ni^{3+} site fractions that are not represented in free energy vs composition curves such as Fig. 3. These are determined by valence neutrality, structure conservation, and oxygen equilibrium as discussed above. The site fractions of these species as a function of chromium concentration are plotted in Fig. 4. In the limit as the chromium concentration goes to zero, we would see that $\chi_{Ni^{3+}} \to 2\chi_{V_a}$ in accordance with the valence neutrality constraint, and χ_{V_a} goes to the native cation vacancy concentration of pure rocksalt ($Fm\bar{3}m$) NiO for the given temperature and oxygen chemical potential. As the concentration of chromium increases the site fraction of Ni^{3+} decreases and χ_{V_a} also increases. The concentrations also depend upon temperature and oxygen chemical potential, but the qualitative shape does not change. In the limit of chromium concentration approaching 1 the vacancy concentration approaches 0.5 as expected for valence neutrality; Cr^{3+} is replacing Ni^{2+}.

3.2. Density functional theory calculations

Most thermodynamic databases are limited to compounds for which experimental data is available. One can go beyond this using density functional methods, but some care is needed particularly

for transition metal oxides. There are inevitable compromises with the functional used. The most common functional currently used is the PBE generalized gradient approximation (GGA) [52], which, while it often gives very good results, leads to too much covalency (too little ionicity). Probably the best current approach is to use a metaGGA, for instance the recent SCAN functional [53,54]. This improves the description of molecular oxygen and is significantly better for surfaces or interfaces, but this does not fully solve the ionicity problem. The classic method for correcting this is the LDA+U method [55,56]. In general LDA+U increases the ionicity of the bonding; unfortunately the method requires a number for the value of the Hubbard U that is difficult to determine independently, and will depend upon the local environment and spin state so is not a global parameter. A better, more modern approach is to use higher-level orbital-DFT methods such as hybrids (e.g. [57–61]) where fractional exact exchange terms are added, but this only comes at considerable computational cost. A fast compromise is to use an on-site approach [62–64], which calculates an exact exchange correction within the atomic spheres, and is only about ten percent slower than the PBE GGA. Of particular importance here, the method auto-adapts to changes in coordination and spin state so can be applied with reasonable confidence across a wide range of compositions and structures.

DFT calculations were performed with the all-electron augmented plane wave + local orbitals WIEN2K code [65] for different Ni and Cr concentrations in either rocksalt ($Fm\bar{3}m$) or corundum ($R\bar{3}c$) structures; crystallographic information files (CIF) for all the low energy structures considered are included as Supplemental material. (Structures which were tested but found to be of significantly higher energy have not been included.) Technical parameters for these calculations were use of the PBE functional [52] exchange-correlation potential, a hybrid fraction of 0.25 for the d-electrons of both Ni and Cr using an on-site approach [62–64], k-point densities in reciprocal space of 100–200 nm^3, oversampling of the exchange-correlation potential and otherwise conventional parameters with atomic positions and densities converged with a parallel fixed-point algorithm [66]. All calculations were performed with the DFT optimized lattice parameters as a function of volume, preserving the space group. In addition to the densities of states which will be shown later, to assist in interpretation the bond-valence sums were analyzed [67,68], since interpretation of valence is normally based upon these.

Converting DFT energies to thermodynamic numbers for systems containing both metals and oxides is not simple. Hybrid calculations improve the accuracy of the exchange contributions which are important for oxides, but without a balancing correlation term leads to a worse descriptions of metals. To avoid inconsistencies with the treatment of the metal reference in the DFT calculations, the known heats of formation for nickel oxide and chromia were used as references. To avoid issues with the bond energy of molecular oxygen the standard heat of formation of atomic oxygen was used in addition to the energy of an isolated oxygen atom in a tetragonal $8.4 \times 8.4 \times 10.0$ Angstrom unit cell. Based upon tests the hybrid fraction of 0.25 used gave values for the relative heats of formation of Ni_2O_3 and the spinel $NiCr_2O_4$ which were within about 10 kJ/mole. It also gave positions for the atoms in corundum Cr_2O_3 which were in good agreement with experiment; this is an energy-independent cross-validation. Hence the absolute reported values should be accurate to approximately this level – relative values may be slightly better than this. To facilitate comparison with the TD values, the bulk entropy contribution from the dataset of the oxides was used; an average of 57.7 kJ/mole/metal atom which is close to that for NiO (58.4) and Cr_2O_3 (57.7), and the free energies of formation at temperature were corrected using the tabulated free energy of molecular oxygen. All the DFT energies presented below are 1000 K and one atmosphere of oxygen; values at STP are given in Supplemental Table 1. The free entropy of mixing was also considered, but since this is only a few kJ/mole it would not show on the plots so has not been included.

We note that with the absolute energies referenced as detailed above, the DFT numbers are constrained to match the known thermodynamics of pure rocksalt NiO and corundum Cr_2O_3, and are also constrained to be quite accurate for corundum Ni_2O_3 and the spinel $NiCr_2O_4$. They are therefore a good test of the accuracy of the thermodynamic database extrapolation of the energies for the solute captured compositions. As will be seen, the database values are surprisingly good for rocksalt, but not so good for other cases.

Four cases were considered:

1. Ni^{2+} and Cr^{3+} in a cubic rocksalt structure ($Fm\bar{3}m$) with half a Ni^{2+} vacancy per Cr^{3+} to preserve valence neutrality.
2. Ni^{2+} and Cr^{3+} in the corundum structure ($R\bar{3}c$) with 1.5 Ni^{2+} per removed Cr^{3+} to preserve valence neutrality.
3. Ni^{3+} and Cr^{3+} in the corundum structure ($R\bar{3}c$) with site substitution. It turned out that these are better described as combinations of Ni^{2+} with Cr^{3+} and Cr^{4+} as discussed below.
4. Ni^{2+} and Cr^{2+} in the rocksalt structure ($Fm\bar{3}m$) with site substitution.

It was found that the structures were lowest in energy when they followed the antiferromagnetic ordering of the parent rocksalt ($Fm\bar{3}m$) NiO or corundum ($R\bar{3}c$) Cr_2O_3, except for case 4 where the lowest energy state in the limiting case of CrO was ferromagnetic. This indicates a non-magnetic ground states which is consistent with results for $NiCrO_3$ in the literature [45,47]. In some cases different structures with the same fraction of cations were calculated; differences in most cases were less than 10 kJ/mole/metal atom and reflect the smaller ordering energies. For the spinel ($Fd\bar{3}mZ$), a search over antiferromagnetic orderings was performed, as this is not well defined in the current literature [69–72]. The lowest energy configuration of the spinel was anti-ferromagnetic ordered on the twin-related (100) or (010) planes for both Ni^{2+} and Cr^{3+}.

Full details of the atomic positions are given in the Supplemental Material. All the structures herein were somewhat ordered, and most were good insulators with band gaps of 2–3 eV. Experimental samples are not as well ordered, and in many cases will have significant disorder, i.e. random site occupancy of chromium, nickel and cation vacancies satisfying valence neutrality. The effect of disorder will be discussed in more detail elsewhere [31].

The energies are summarized in Fig. 5 for the two limits of normalized per metal atom and normalized per oxygen atom; full values for the energies are provided in Supplemental Tables 1–4. The agreement between the TD and DFT calculations is quite good, particularly when one considers that the TD values for the rocksalt structure is an extrapolation from small chromium content to a pure chromium rocksalt.

Interpretation of the two normalizations and incorporation of oxygen chemical potential requires further discussion. The normalizations correspond to different physical limits, which in turn correspond to different material systems and diffusion limits:

a) For the limit of only cation vacancy diffusion when the metal/oxide interface is stationary and growth is occurring at the outer surface, the controlling thermodynamic term is the change *per metal atom* as these are the active species – i.e. the normalization on the left. This is relevant to, for instance, the growth of rocksalt where cation vacancies are known to dominate the diffusion [73,74]. The relative free energy changes will vary with oxygen chemical potential because the oxygen content per metal atom varies across the plots for the Ni^{2+}/Cr^{3+} systems. (It does not for Ni^{2+}/Cr^{2+} or Ni^{3+}/Cr^{3+}.)
b) For the limit of only anion diffusion, when the outer surface is stationary and growth is occurring at the inner surface, the

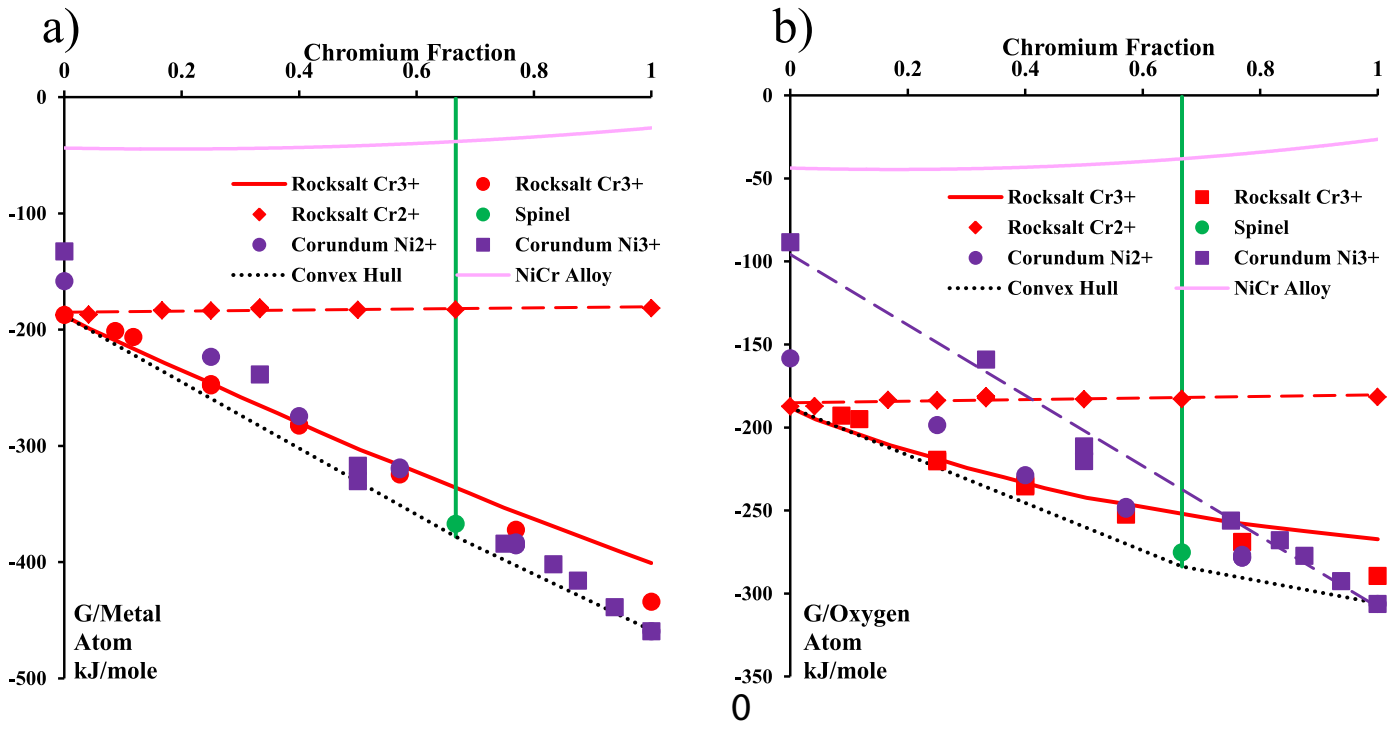

Fig. 5. Plot of the free energy of the different crystallographic phases at 1000 K and one atmospheric of oxygen in kJ/mole as color coded, as a function of Cr composition. Points are from the DFT calculations, solid lines from the thermodynamic database, the convex hull is shown as a dotted line and dashed lines are to guide the eye. In (a) on the left is shown the results normalized per metal atom, in (b) on the right with a normalization per oxygen atom (proportional to per unit volume of oxide). The two cases are relevant to different diffusing species as described in the text. (For interpretation of the references to color in this figure legend, the reader is referred to the web version of this article.)

controlling thermodynamic term is the change *per oxygen atom* as these are the active species – i.e. the normalization on the right. This is relevant to, for instance, the growth of corundum where the dominant diffusing species are oxygen point defects [75–77]. The free energies of the oxide will all shift vertically with oxygen chemical potential, but the relative order will not change.

For cases when both cation and anion diffusing species are present an appropriate intermediate scaling should be needed. We note that there are significant differences therefore between the driving forces for solute capture depending upon what are the active diffusing species. From the plots one would expect a higher probability for solute capture for rocksalt structures (left) than for corundum (right) since the relevant oxides are closer to the convex hull of the pure, lowest free energy phases NiO, $NiCr_2O_4$ and Cr_2O_3, which is borne out in experimental data which will be described further elsewhere.

Some additional details are briefly discussed below; some additional points about the relevance of the results to interpretation of spectroscopic data are included in the discussion.

Firstly, the density of states of the established end members with both rocksalt and corundum crystallographies are shown in Fig. 6; these are established phases so will not be discussed further, and are given for reference purposes only. The bond lengths are summarized in Table 1 for the end members. For the same valence state Cr is about 2.5% larger, and the 3+ valence states are 6–8% smaller. For later reference, the oxygen bond length for Cr^{4+} based upon CrO_2 was 1.924 Angstroms. This means that there will always be mismatches between the cation-oxygen bond distances, with, for instance, the Cr^{3+} in rocksalt the distances are always slightly larger than optimal, the Ni^{2+} slightly smaller. Elongating the bonds leads to a reduction in the local band gap; reducing will increase the effective local band gap so Cr^{3+} rocksalt will tend to dominate the valence and conduction band edges which was observed in general as detailed below.

Table 1
summary of (DFT) bond lengths in end member oxides.

	Rocksalt	Corundum	Spinel
Ni2+	2.105	2.07	2.016
Ni3+	–	1.952	–
Cr2+	2.161	–	–
Cr3+	1.978	1.998	2.039

3.2.1. *Rocksalt* ($Fm\bar{3}m$) *structures with* Cr^{3+} *and* Ni^{2+}

The rocksalt structures follow approximately the thermodynamic database values, slightly higher in energy for low chromium content and slightly lower for high chromium content. (Without experimental data it is unclear which of the two approaches is more accurate.). As shown in the density of states plot (DOS) of Fig. 7 for a low content $Ni_{21}Cr_2O_{24}$ as well as an intermediate $Ni_9Cr_6O_{18}$ the chromium is in a high-spin state and tends to define the edges of the valence and conduction bands. Both the chromium and nickel remain as charge-transfer insulators. The end member is between 26 (DFT) and 60 (TD) kJ/mole higher in energy than the corundum Cr_2O_3 phase at 1000 K.

3.2.2. *Corundum* ($R\bar{3}c$) *structures with* Cr^{3+} *and* Ni^{2+}

Similar to the rocksalt of 3.2.1, the chromium and nickel retain their local charge-transfer insulator DOS as shown in Fig. 6 for the end member corundum NiO and in Fig. 8 for $Ni_6Cr_8O_{18}$. For the later, the band edges are dominated by the Cr states, as in other cases. The end member is approximately 30 kJ/mole and per metal atom higher in energy than the pure NiO rocksalt structure at both STP and 1000 K. As mentioned earlier in Section 3.1 the TD has inaccurate numbers for these compounds.

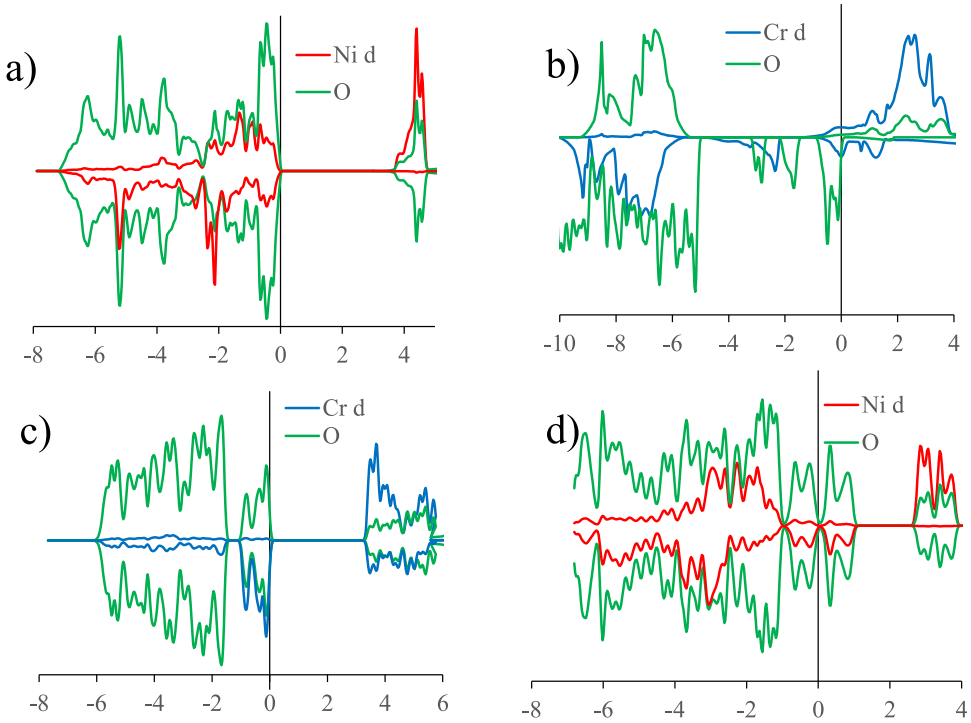

Fig. 6. Density of states for the end members in both space groups, Rocksalt (a) $Ni^{2+}O$, (b) $Cr^{2}+O$ and Corundum (c) $Cr^{3+}{}_2O_3$, (d) $Ni^{3+}{}_2O_3$, color coded according to the legend. Up spins are above the axis and down spins below, with the *x* axis in eV using the Fermi energy as the origin, *y*-axis is unitless. (For interpretation of the references to color in this figure legend, the reader is referred to the web version of this article.)

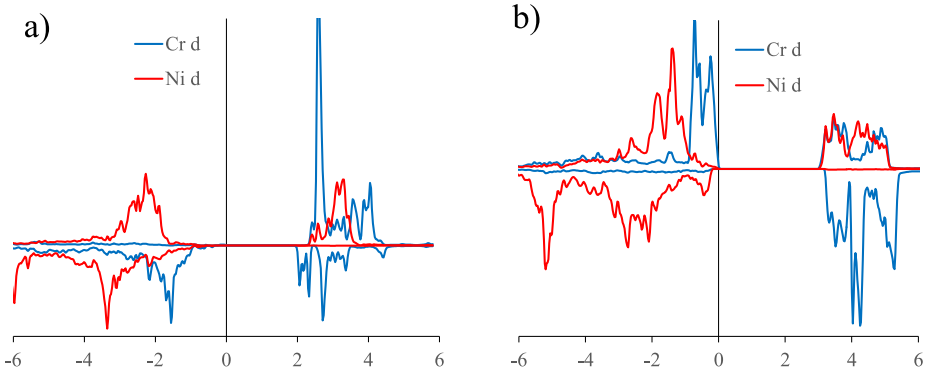

Fig. 7. Density of states for the Ni and Cr 3d states, for rocksalt structures with Cr^{3+}, in (a) $Ni_{21}Cr_2O_{24}$ and (b) $Ni_9Cr_6O_{18}$, color coded according to the legend. The conduction band edges are dominated by Cr states in both cases, the valence edge is dominated by oxygen states (not shown) at low Cr concentrations and by the Cr at higher concentrations. Up spins are above the axis and down spins below, with the *x* axis is in eV using the Fermi energy as the origin, *y*-axis is unitless. (For interpretation of the references to color in this figure legend, the reader is referred to the web version of this article.)

3.2.3. Corundum ($R\bar{3}c$) structures with Cr^{3+} and Ni^{3+}

The energies for substitution of Ni^{3+} for Cr^{3+} are sensitive to the functional used; it is a well-known result that in the simple PBE function incorrectly predicts that Ni_2O_3 in the corundum structure is significantly more stable at STP than rocksalt NiO. For the calculations herein the end member of corundum NiO is 0.5 kJ/mole higher in energy than rocksalt at STP, and 50 kJ/mole higher at 1000 K.

This set of structures is the most complex, and Fig. 9 shows the DOS a low nickel content $NiCr_{15}O_{24}$ a midpoint $NiCrO_3$ in Fig. 9a and b, respectively. At the low Ni levels of $NiCr_{15}O_{24}$ the compound is a p-type semiconductor with the hole split between a Ni atom at, before relaxation, (0,0,0) and three chromium atoms at (0,0,1/2). The nickel atom is best described as having a mixed valence of approximately $Ni^{2.4+}$ with some of the hole located on three adjacent Cr atoms so that they would be described as $Cr^{3.2+}$; the Ni^{3+} is partially oxidizing the Cr^{3+} towards Cr^{4+}. This oxidation is more notable in the midpoint NiCrO3 which is an insulator best described as $Ni^{2+}Cr^{4+}O^{2-}{}_3$. Almost all the other structures considered also show evidence for Cr^{4+} rather than Ni^{3+}. In the limit of Ni_2O_3, because there is no chromium available the lowest energy configuration is a degenerate p-type semiconductor (metal). These trends are consistent with the thermodynamic data for the oxides; based upon the standard heats of formation the reaction

$$Ni^{3+}{}_2O_3 + Cr^{3+}{}_2O_3 \rightarrow 2Ni^{2+}O + 2Cr^{4+}O_2$$

has an enthalpy change of −11.7 kJ/mole per metal atom at STP, i.e. is favorable.

3.2.4. Spinel ($Fd\bar{3}mZ$)

As mentioned previously, while there have been prior DFT calculations of the spinel Cr_2NiO_4 [69–72], it does not appear that a complete search over spin states was performed. With DFT calculations different spin states are often local minima, so incorrect

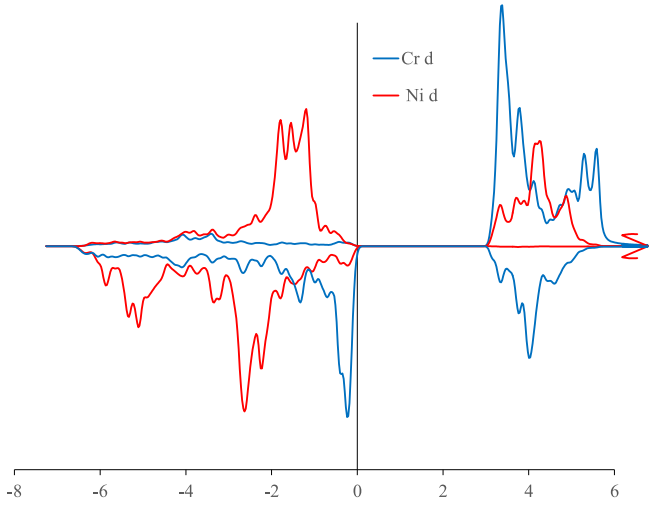

Fig. 8. Density of states for the Ni and Cr 3d states, for corundum structure with Ni^{2+}, here $Ni_6Cr_8O_{18}$, color coded according to the legend. The valence and conduction band edges are dominated by Cr states. Up spins are above the axis and down spins below, with the *x* axis is in eV using the Fermi energy as the origin, *y*-axis is unitless. (For interpretation of the references to color in this figure legend, the reader is referred to the web version of this article.)

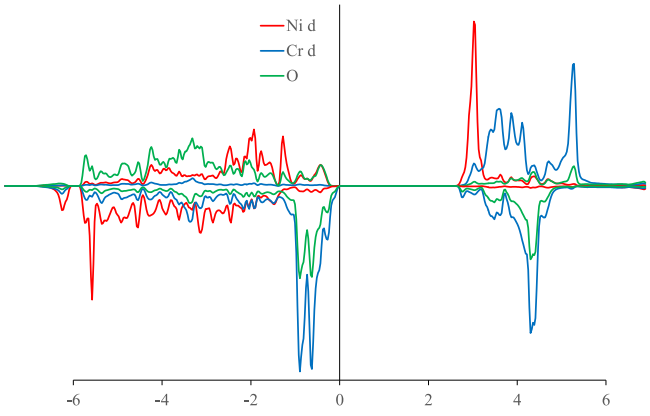

Fig. 10. Density of states for the spinel $NiCr_2O_4$ showing the Ni and Cr 3d-states and the O 2p states, color coded according to the legend. Up spins are above the axis and down spins below, with the *x* axis is in eV using the Fermi energy as the origin, *y*-axis is unitless. (For interpretation of the references to color in this figure legend, the reader is referred to the web version of this article.)

conclusions can be reached. Based upon a search, the antiferromagnetic cell belongs to the spacegroup Imm2, with DFT lattice parameters of $6.03 \times 6.03 \times 8.53$ Å. Both the Ni^{2+} and Cr^{3+} are in the expected high-spin states, and the DOS shown in Fig. 10 and shows a valence band edge defined primarily by the filled Cr^{3+} and O^{2-} states, and a conduction band edge defined primarily by the empty Ni^{2+} states and a (DFT) band gap of 2.59 eV. The agreement between the DFT and TD energies is very good, with the DFT ~10 kJ/mole higher in energy. For completeness we should mention that there is strong experimental evidence for a spinel or inverse spinel Ni_3O_4 [43], so this may not be a line compound.

3.2.5. Rocksalt ($Fm\bar{3}m$) with Ni^{2+} and Cr^{2+}

The chromous based oxide with the slightly anomalous Cr^{2+} state is the exception. The DOS are shown for the compositions $NiCr_{23}O_{48}$ and $NiCrO_2$ in Fig. 11 based upon substitutions into antiferromagnetic NiO. The additional of chromium at low concentrations (1/24) leads to a n-type semiconductor dominated by chromium states at the valence and conduction band edges (Fig. 11a), at high concentrations it is a ferromagnetic metal which is better described as a degenerate n-type doped semiconductor. The energy increases slightly with chromium content. For reducing conditions at the metal/oxide interface it is possible that some metastable Cr^{2+} can be formed, and there are experimental indications of this [28]. It is worth repeating that there is a deep eutectic in the phase diagram close to the composition of rocksalt chromous oxide CrO.

4. Discussion

The results indicate there are a range of (probably) metastable compositions across the whole compositional range for both the rocksalt ($Fm\bar{3}m$) and corundum ($R\bar{3}c$) crystallographies. These form a band which is bounded at the bottom by ordered phases, and we can expect there to be disordered variants above these in energy. As described previously [28] this is not really surprising since there is comparatively little difference in atomic radii across the first transition metal row. This band is almost certainly common for alloys involving first transition metal atoms as indicated by DFT calculations [28]. During high-temperature oxidation or aqueous corrosion this means that variable compositions outside the conventional thermodynamic phases should be expected to be common across the first transition row.

An interesting conceptual issue needs clarification – what element is being captured in which oxide? From a thermodynamic

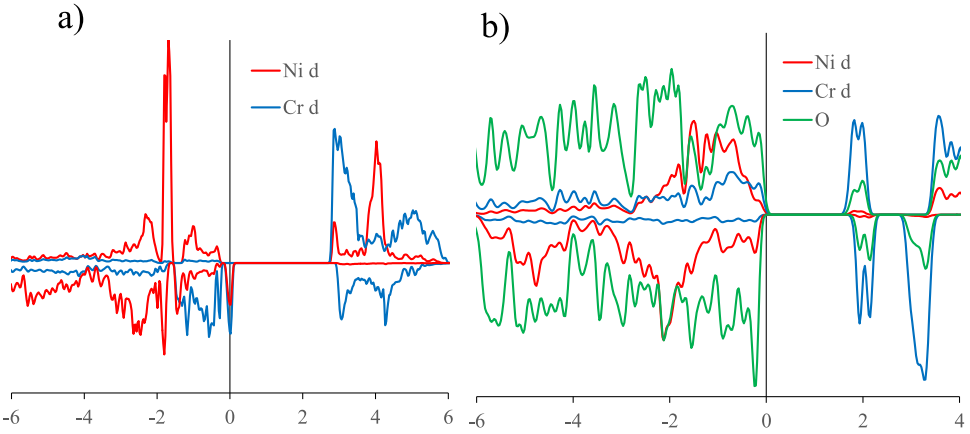

Fig. 9. Density of states for corundum structures with Ni^{3+}: in (a) $NiCr_{15}O_{24}$ and (b) $NiCrO_3$, color coded according to the legend; both are discussed further in the text. Up spins are above the axis and down spins below, with the *x* axis is in eV using the Fermi energy as the origin, *y*-axis is unitless. (For interpretation of the references to color in this figure legend, the reader is referred to the web version of this article.)

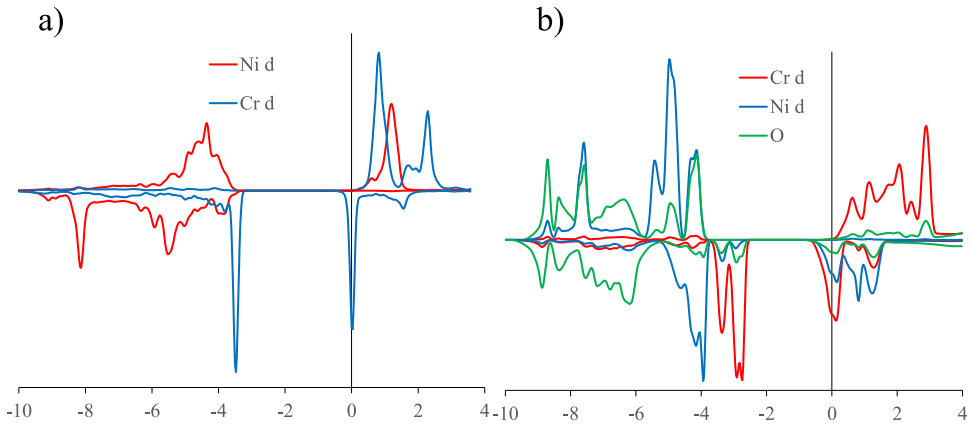

Fig. 11. Density of states in (a) for $NiCr_{23}O_{48}$ showing just the 3d-states of a Cr atom at (0,0,0) and one of the Ni atoms at, before relaxation, (5/6,2/3,1/3) and in (b) the density of states for the Ni and Cr 3d-states and the O 2p states, color coded as per the legend. Up spins are above the axis and down spins below, with the *x* axis is in eV using the Fermi energy as the origin, *y*-axis is unitless. (For interpretation of the references to color in this figure legend, the reader is referred to the web version of this article.)

viewpoint, in both the rocksalt with Ni^{2+} and Cr^{3+} as well as the corundum with Ni^{2+}/Ni^{3+} and Cr^{3+} the logical choice is the lowest free energy parent, i.e. in both cases nickel (not chromium) is being captured. Slightly different is Cr^{2+} in NiO where the free energy increases with Cr^{2+} content; therefore Cr^{2+} is the captured cation. An alternative view might be to approach from a crystallographic view, in which case one could consider Cr^{3+} or Cr^{2+} as being captured in rocksalt NiO and Ni^{2+} in corundum Cr_2O_3. We believe that it is important to follow the thermodynamics, not the crystallography since otherwise one can be led into inappropriate assumptions as to how the system will evolve.

All the oxides, except those with high concentrations of Cr^{2+} are significantly lower in free energy than the alloy for all compositions, and therefore satisfy one of the two necessary conditions for nonequilibrium solute capture to occur. This is one of the fundamental differences from solute trapping during solidification. In solidification there is a composition and temperature (T_0) where the two free energy curves cross. This implies that the chemical potential of the solute can increase on solidification and thus trapping is possible. In the oxidation case, except at very low partial pressures of oxygen, the free energy curves do not cross for any reasonable compositions, and thus capture always can occur. However, as in the solidification case, the compositions are not given by the equilibrium phase diagram, and thus the composition of the growing oxide depends on the kinetics of the process.

One somewhat important point needs to be made concerning the implications of the DFT results on interpretation of corrosion and oxidation chemistries from spectroscopic methods. It is standard to use known oxides as calibrants, and from these infer the presence of local co-ordination approaches such as x-ray photoelectron spectroscopy (e.g. [2,78]). This assumes that the local band structure of the known oxides and unknown corrosion or oxidation products are similar. However, the DFT results indicate that in particular for oxidizing conditions where Ni^{3+} might be expected to occur together with Cr^{3+} such simple interpretations are prone to error. As shown above Ni^{3+} can oxidize Cr^{3+}, and one can have either or both mixed-valence states or Cr^{4+}. This indicates that extreme care is needed in interpreting valence results based just upon spectroscopic information.

One final comment. In this paper we have only focused on the basic description of the thermodynamics and ordered structures during nonequilibrium solute capture. These lay the groundwork for one of the two conditions, and also for the basic properties of these unusual oxides. While estimates of the kinetic condition (see [28]) suggest that capture will occur for many cases of high-temperature oxidation and almost all cases of aqueous corrosion, this is an topic which requires further work. We have also not considered the role of nucleation of the different oxides which should be expected to show strong crystallographic dependencies due to epitaxial effects as well as whether polar or non-polar interfaces are involved. Another issue that merits attention is how the captured oxide phases will evolve with time, which will be important for understanding the microstructure and corrosion/oxidation resistance of thicker oxide films and also has significant technological relevance; these we will also leave for future work.

5. Conclusions

The very early stages of oxide growth on an alloy, when several oxide phases can compete to form multilayer structures, are important in predicting the long-term corrosion resistance of alloys. Previous models have assumed that the most thermodynamically stable oxide phases form first and that phase boundaries are in local equilibrium. Given the interfacial velocities of many oxidation processes this is not the case. Evaluation of the thermodynamics of the Ni–Cr–O system from both a database approach and via density functional theory calculations indicate that there are a wide range of compounds which can form. For the specific case of the Ni–Cr–O system there will be considerable solute capture of nickel in either rocksalt or corundum crystallographies, and even possible capture of Cr^{2+} in rocksalt. These oxides range from good insulators to n-type or p-type semiconductors or degenerate metals depending upon the composition, and can also contain Cr^{4+} ions instead of Ni^{3+} under stronger oxidizing conditions. Care is therefore needed in the interpretation of spectroscopic data on the valences, and also on the semiconducting properties of thin oxide films.

Acknowledgments

This work was supported by the Office of Naval Research MURI Grant No. N00014-16-1-2280. We are grateful to J. H. Perepezko for many helpful insights during the preparation of this manuscript.

Supplementary materials

Supplementary material associated with this article can be found, in the online version, at doi:10.1016/j.actamat.2019.09.043.

References

[1] A. Atkinson, Transport processes during the growth of oxide-films at elevated-temperature, Rev. Mod. Phys. 57 (2) (1985) 437–470.

[2] N. Winograd, W.E. Baitinger, J.W. Amy, J.A. Munarin, X-ray photoelectron spectroscopic studies of interactions in multicomponent metal and metal oxide thin films, Science 184 (4136) (1974) 565–567.
[3] R.D. Willenbruch, C.R. Clayton, M. Oversluizen, D. Kim, Y. Lu, An xps and electrochemical study of the influence of molybdenum and nitrogen on the passivity of austenitic stainless-steel, Corros. Sci. 31 (1990) 179–190.
[4] P. Saltykov, O. Fabrichnaya, J. Golczewski, F. Aldinger, Thermodynamic modeling of oxidation of Al-Cr-Ni alloys, J. Alloys Compd. 381 (1–2) (2004) 99–113.
[5] B. Ingham, S.C. Hendy, N.J. Laycock, M.P. Ryan, Estimates of thermodynamic stability of iron-chromium spinels in aqueous solution based on first-principles calculations, Electrochem. Solid State Lett. 10 (10) (2007) C57–C59.
[6] B. Beverskog, I. Puigdomenech, Pourbaix diagrams for the ternary system of iron-chromium-nickel, Corrosion 55 (11) (1999) 1077–1087.
[7] J.E. Croll, G.R. Wallwork, High-temperature oxidation of iron-chromium-nickel alloys containing 330percent chromium, Oxid. Met. 4 (3) (1972) 121–139.
[8] A.D. Dalvi, D.E. Coates, A review of the diffusion path concept and its application to the high-temperature oxidation of binary alloys, Oxid. Met. 5 (2) (1972) 113–135.
[9] J.J. Gilman, Oxide surface films on metal crystals, Science 306 (5699) (2004) 1134–1135 author reply 1134-5.
[10] S.E. Ziemniak, L.M. Anovitz, R.A. Castelli, W.D. Porter, Thermodynamics of Cr_2O_3, $FeCr_2O_4$, $ZnCr_2o_4$, and $CoCr_2O_4$, J. Chem. Thermodyn. 39 (11) (2007) 1474–1492.
[11] L. Kaufman, J.H. Perepezko, K. Hildal, J. Farmer, D. Day, N. Yang, D. Branagan, Transformation, stability and pourbaix diagrams of high performance corrosion resistant (HPCRM) alloys, Calphad 33 (1) (2009) 89–99.
[12] R. Kirchheim, B. Heine, H. Fischmeister, S. Hofmann, H. Knote, U. Stolz, The passivity of iron-chromium alloys, Corros. Sci. 29 (7) (1989) 899–917.
[13] L. Zhang, D.D. Macdonald, Segregation of alloying elements in passive systems - I. XPS studies on the Ni-W system, Electrochim. Acta 43 (18) (1998) 2661–2671.
[14] J.E. Castle, K. Asami, A more general method for ranking the enrichment of alloying elements in passivation films, Surf. Interface Anal. 36 (3) (2004) 220–224.
[15] D.D. Macdonald, The role of passivity in the corrosion resistance of metals and alloys, Afinidad 62 (519) (2005) 498–504.
[16] C. Wagner, Oxidation of alloys involving noble metals, J. Electrochem. Soc. 103 (10) (1956) 571–580.
[17] C. Wagner, Theoretical analysis of the diffusion processes determining the oxidation rate of alloys, J. Electrochem. Soc. 99 (10) (1952) 369–380.
[18] B. Chattopadhyay, G.C. Wood, The transient oxidation of alloys, Oxid. Met. 2 (4) (1970) 373–399.
[19] J.C. Yang, E. Schumann, I. Levin, M. Ruhle, Transient oxidation of NiAl, Acta Mater. 46 (6) (1998) 2195–2201.
[20] J. Doychak, J.L. Smialek, T.E. Mitchell, Transient oxidation of single-crystal beta-nial, Metall. Trans. A – Phys. Metall. Mater. Sci. 20 (3) (1989) 499–518.
[21] V.K. Tolpygo, D.R. Clarke, Microstructural study of the theta-alpha transformation in alumina scales formed on nickel-aluminides, Mater. High Temp. 17 (1) (2000) 59–70.
[22] G.C. Rybicki, J.L. Smialek, Effect of the theta-alpha-Al2O3 transformation on the oxidation behavior of beta-NiAl + Zr, Oxid. Met. 31 (3–4) (1989) 275–304.
[23] W. Ostwald, Studien über die bildung und umwandlung fester körper, Z. Phys. Chem. 22U (1) (1897) 19.
[24] I.N. Stranski, D. Totomanow, Seed formation speed and ostwald's step rule, Z. Phys. Chem.-Abteilung A – Chem. Thermodyn. Kinet. Elektrochem. Eigenschaftslehre 163 (5/6) (1933) 399–408.
[25] R.A. Vansanten, The Ostwald step rule, J. Phys. Chem. 88 (24) (1984) 5768–5769.
[26] J. Nyvlt, The Ostwald rule of stages, Cryst. Res. Technol. 30 (4) (1995) 443–449.
[27] N. Niekawa, M. Kitamura, Role of epitaxy-mediated transformation in Ostwald's step rule: a theoretical study, Crystengcomm 15 (35) (2013) 6932–6941.
[28] X.X. Yu, A. Gulec, Q. Sherman, K.L. Cwalina, J.R. Scully, J.H. Perepezko, P.W. Voorhees, L.D. Marks, Nonequilibrium solute capture in passivating oxide films, Phys. Rev. Lett. 121 (14) (2018) 145701.
[29] J.C. Baker, J.W. Cahn, Solute trapping by rapid solidification, Acta Metall. Mater. 17 (5) (1969) 575–578.
[30] L.V. Ramanathan, P.W. Voorhees, In preparation (2019).
[31] E. Long, X.-X. Yu, L.D. Marks, Understanding the Electronic Structure of Nonequilibrium Solute Oxides, In preparation (2019).
[32] J.C. Baker, J.W. Cahn, in: Thermodynamics of Solidification, Solidification, American Society for Metals, Metals Park, OH, 1971, pp. 23–58.
[33] W.J. Boettinger, S.R. Coriell, R.F. Sekerka, Mechanisms of microsegregation-free solidification, Mater. Sci. Eng. 65 (1) (1984) 27–36.
[34] P. Galenko, Solute trapping and diffusionless solidification in a binary system, Phys. Rev. E Stat. Nonlinear Soft Matter Phys. 76 (3 Pt 1) (2007) 031606.
[35] M.J. Aziz, Model for solute redistribution during rapid solidification, J. Appl. Phys. 53 (2) (1982) 1158–1168.
[36] M.E. Gurtin, P.W. Voorhees, The thermodynamics of evolving interfaces far from equilibrium, Acta Mater. 44 (1) (1996) 235–247.
[37] D.S. Walters, G.P. Wirtz, Kinetics of cation ordering in magnesium ferrite, J. Am. Ceram. Soc. 54 (11) (1971) 563–566.
[38] K.D. Becker, F. Rau, High-temperature ligand-field spectra in spinels – cation disorder and cation kinetics in $NiAl_2O_4$, Phys. Chem. Chem. Phys. 91 (11) (1987) 1279–1282.
[39] K. Sujata, T.O. Mason, Kinetics of cation redistribution in ferrospinels, J. Am. Cerami. Soc. 75 (3) (1992) 557–562.
[40] N. Kashii, H. Maekawa, Y. Hinatsu, Dynamics of the cation mixing of $MgAl_2O_4$ and $ZnAl_2O_4$ spinel, J. Am. Ceram. Soc. 82 (7) (1999) 1844–1848.
[41] S.A.T. Redfern, R.J. Harrison, H.S.C. O'Neill, D.R.R. Wood, Thermodynamics and kinetics of cation ordering in $MgAl_2O_4$ spinel up to 1600 °C from in situ neutron diffraction, Am. Mineral. 84 (3) (1999) 299–310.
[42] J.M. Shi, K.D. Becker, Kinetics and thermodynamics of cation site-exchange reaction in olivines, Solid State Ionics 181 (11–12) (2010) 473–478.
[43] M.I. Buckett, L.D. Marks, Electron-irradiation damage in NiO, Surf. Sci. 232 (3) (1990) 353–366.
[44] J.R. Taylor, A.T. Dinsdale, A thermodynamic assessment of the Ni-O, Cr-O and Cr-Ni-O systems using the ionic liquid and compound energy models, Z. Metall. 81 (5) (1990) 354–366.
[45] B.L. Chamberland, W.H. Cloud, Preparation and properties of $NiCrO_3$, J. Appl. Phys. 40 (1) (1969) 434–435.
[46] K.W. Lee, W.E. Pickett, Compensated half-metallicity in the trigonally distorted perovskite $NiCrO_3$, Phys. Rev. B 83 (18) (2011) 180406.
[47] Y. Qian, H.P. Wu, Y.Z. Liu, J. Lu, R.F. Lu, W.S. Tan, K.M. Deng, C.Y. Xiao, G. Lu, Tuning the physical properties of antiferromagnetic perovskite oxide $NiCrO_3$ by high-pressure from density-functional calculations, Solid State Commun. 170 (2013) 24–29.
[48] A.F. Kusmartseva, A.M. Arevalo-Lopez, M. Halder, J.P. Attfield, Bistability and relaxor ferrimagnetism in off-stoichiometric $NiCrO_3$, J. Magn. Magn. Mater. 443 (2017) 293–299.
[49] V.A. Kurepin, D.A. Kulik, A. Hiltpold, M. Nicolet, Thermodynamic Modelling of Fe-Cr-Ni- Spinel Formation at the Light-Water Reactor Conditions, Paul Scherrer Institute, Villigen, Switzerland, 2002 PSI Report 02-04.
[50] M. Hillert, The compound energy formalism, J. Alloys Compd. 320 (2) (2001) 161–176.
[51] A.T. Dinsdale, Sgte data for pure elements, Calphad 15 (4) (1991) 317–425.
[52] J.P. Perdew, K. Burke, M. Ernzerhof, Generalized gradient approximation made simple, Phys. Rev. Lett. 77 (18) (1996) 3865–3868.
[53] J. Sun, R.C. Remsing, Y. Zhang, Z. Sun, A. Ruzsinszky, H. Peng, Z. Yang, A. Paul, U. Waghmare, X. Wu, M.L. Klein, J.P. Perdew, Accurate first-principles structures and energies of diversely bonded systems from an efficient density functional, Nat. Chem. 8 (9) (2016) 831–836.
[54] J. Sun, A. Ruzsinszky, J.P. Perdew, Strongly constrained and appropriately normed semilocal density functional, Phys. Rev. Lett. 115 (3) (2015) 036402.
[55] V.I. Anisimov, F. Aryasetiawan, A.I. Lichtenstein, First-principles calculations of the electronic structure and spectra of strongly correlated systems: the lda+u method, J. Phys. – Condens. Matter 9 (4) (1997) 767–808.
[56] V.V. Anisimov, J. Zaanen, O.K. Andersen, Band theory and mott insulators: Hubbard u instead of stoner I, Phys. Rev. B Condens. Matter 44 (3) (1991) 943–954.
[57] A.D. Becke, Density-functional thermochemistry. 3. The role of exact exchange, J. Chem. Phys. 98 (7) (1993) 5648–5652.
[58] C. Adamo, V. Barone, Toward reliable density functional methods without adjustable parameters: the PBE0 model, J. Chem. Phys. 110 (13) (1999) 6158–6170.
[59] J. Heyd, G.E. Scuseria, M. Ernzerhof, Hybrid functionals based on a screened Coulomb potential, J. Chem. Phys. 118 (18) (2003) 8207–8215.
[60] J. Heyd, G.E. Scuseria, M. Ernzerhof, Hybrid functionals based on a screened Coulomb potential (vol 118, pg 8207, 2003), J. Chem. Phys. 124 (21) (2006) 219906.
[61] F. Tran, P. Blaha, Implementation of screened hybrid functionals based on the Yukawa potential within the Lapw basis set, Phys. Rev. B 83 (23) (2011) 235118.
[62] P. Novak, J. Kunes, L. Chaput, W.E. Pickett, Exact exchange for correlated electrons, Phys. Status Solidi B 243 (3) (2006) 563–572.
[63] F. Tran, P. Blaha, K. Schwarz, P. Novak, Hybrid exchange-correlation energy functionals for strongly correlated electrons: applications to transition-metal monoxides, Phys. Rev. B 74 (15) (2006) 155108.
[64] F. Tran, J. Kunes, P. Novak, P. Blaha, L.D. Marks, K. Schwarz, Force calculation for orbital-dependent potentials with fp-(l)apw plus lo basis sets, Comput. Phys. Commun. 179 (11) (2008) 784–790.
[65] P. Blaha, K. Schwarz, G.K.H. Madsen, D. Kvasnicka, J. Luitz, R. Laskowsji, F. Tran, L.D. Marks, An Augmented Plane Wave + Local Orbitals Program for Calculating Crystal Properties, Techn. Universitat Wien, Austria, 2018.
[66] L.D. Marks, Fixed-Point optimization of atoms and density in dft, J. Chem. Theory Comput. 9 (6) (2013) 2786–2800.
[67] I.D. Brown, D. Altermatt, Bond-valence parameters obtained from a systematic analysis of the inorganic crystal-structure database, Acta Crystallogr. B 41 (Aug) (1985) 244–247.
[68] I.D. Brown, Recent developments in the methods and applications of the bond valence model, Chem. Rev. 109 (12) (2009) 6858–6919.
[69] F.T. Docherty, A.J. Craven, D.W. McComb, J. Skakle, ELNES investigations of the oxygen K-edge in spinels, Ultramicroscopy 86 (3–4) (2001) 273–288.
[70] K. Tomiyasu, I. Kagomiya, Magnetic structure of nicr2o4 studied by neutron scattering and magnetization measurements, J. Phys. Soc. Jpn. 73 (9) (2004) 2539–2542.
[71] D.A. Eustace, D.W. McComb, A.J. Craven, Probing magnetic order in eels of chromite spinels using both multiple scattering (FEFF8.2) and DFT (WIEN2k), Micron 41 (6) (2010) 547–553.
[72] I. Efthimiopoulos, I. Khatri, Z.T.Y. Liu, S.V. Khare, P. Sarin, V. Tsurkan, A. Loidl, D.Z. Zhang, Y.J. Wang, Universal link of magnetic exchange and structural behavior under pressure in chromium spinels, Phys. Rev. B 97 (18) (2018) 184435.
[73] M. O'Keeffe, W.J. Moore, Diffusion of oxygen in single crystals of nickel oxide, J. Phys. Chem. 65 (8) (1961) 1438–1439.

[74] A. Atkinson, R.I. Taylor, The self-diffusion of ni in nio and its relevance to the oxidation of Ni, J. Mater. Sci. 13 (2) (1978) 427–432.
[75] X. Ledoux, S. Mathieu, M. Vilasi, Y. Wouters, P. Del-Gallo, M. Wagner, Oxide growth characterization during short-time oxidation of a commercially available chromia-forming alloy (HR-120) in air at 1050 °C, Oxid. Met. 80 (1–2) (2013) 25–35.
[76] A.C.S. Sabioni, E.A. Malheiros, V. Ji, F. Jomard, W.A.D. Macedo, P.L. Gastelois, Ion diffusion study in the oxide layers due to oxidation of aisi 439 ferritic stainless steel, Oxid. Met. 81 (3–4) (2014) 407–419.
[77] S. Voyshnis, A. Seyeux, S. Zanna, B. Martin-Cabanas, T. Couvant, P. Marcus, Oxide layer growth on nickel-base alloy surfaces in high temperature water and in O2 studied by tof-sims with isotopic tracers, Corros. Sci. 145 (2018) 212–219.
[78] A. Machet, A. Galtayries, S. Zanna, L. Klein, V. Maurice, P. Jolivet, M. Foucault, P. Combrade, P. Scott, P. Marcus, XPS and STM study of the growth and structure of passive films in high temperature water on a nickel-base alloy, Electrochim. Acta 49 (22–23) (2004) 3957–3964.